Supplemental Material for: Imaging of Submicroampere Currents in Bilayer Graphene Using a Scanning Diamond Magnetometer

M. L. Palm[1,†], W. S. Huxter[1,†], P. Welter[1], S. Ernst[1], P. J. Scheidegger[1], S. Diesch[1], K. Chang[1,‡], P. Rickhaus[1,§], T. Taniguchi[2], K. Watanabe[3], K. Ensslin[1,4], and C. L. Degen[1,4]

[1]*Department of Physics, ETH Zurich, Otto Stern Weg 1, 8093 Zurich, Switzerland;*

[2]*International Center for Materials Nanoarchitectonics, National Institute for Materials Science, 1-1 Namiki, Tsukuba 305-0044, Japan;*

[3]*Research Center for Functional Materials, National Institute for Materials Science, 1-1 Namiki, Tsukuba 305-0044, Japan; and*

[4]*Quantum Center, ETH Zurich, 8093 Zurich, Switzerland.*[*]

(Dated: April 11, 2022)

[*] degenc@ethz.ch; [†]These authors contributed equally.; [‡]Present address: Aeva Inc., 555 Ellis St., Mountain View, CA 94043, USA.; [§]Present address: Qnami AG, Hofackerstrasse 40B, 4132 Muttenz, Switzerland.

1. MATERIALS AND METHODS

1.1. Device fabrication

All flakes of the van-der-Waals stack are mechanically exfoliated onto silicon substrate chips with a 90 nm oxide layer. Preselected flakes are subsequently picked up with a polymer stamp in a dry transfer process [25, 26] in an argon atmosphere (1. top hBN 2. (bilayer) graphene 3. bottom hBN 4. graphite) and deposited on a pre-patterned 3x3 mm^2 substrate chip. The remaining polymer residues are then dissolved in dichloromethane. The final stack is annealed at 350 °C for 3h in an argon atmosphere. We define electrical contacts in an e-beam lithography step using a bilayer of PMMA 50k (AR-P 630 series) and PMMA 950k (AR-P 670 series). We use an additional conductive polymer (AR PC 5090.02) as a top layer to mitigate charging during the e-beam exposure. To create a one-dimensional contact to the graphene sheet [25], we etch away sections of the top h-BN flake and partially the bottom h-BN flake (reactive ion etching with CHF_3/O_2). The Cr/Au contacts are then deposited with an electron beam evaporator and the excessive metal is removed in a lift-off process. The process for patterning the device is very similar with the exception that the metal deposition step is omitted We contact the finished device with Al bond wires.

1.2. Experimental setup

The scanning diamond magnetometer consists of a confocal microscope to read out the photo-luminescence of the NV center and an atomic force microscope to scan the sample with the diamond sensor. The diamond sensor is attached to a quartz tuning fork in an amplitude modulated shear-mode configuration [30]. The degeneracy of the $m_S = \pm 1$ states of the NV center is lifted by a bias field that is created by a movable permanent magnet beneath the sample holder. Microwave pulses are applied via a bond wire positioned close to the NV center. During a magnetometry scan, only the sample stage is moved (except for occasional optical re-alignment). The laser pulses are generated by a pulsed diode laser that was designed in-house. An arbitrary waveform generator (Spectrum DN2.663-04) synchronizes the laser pulses, the microwave pulses and the voltage signals sent to the graphene device. The device current is amplified with a transimpedance amplifier and recorded with the data acquisition module of a lock-in amplifier (Zurich Instruments MFLI). The photon signal of

the NV center is captured by a single photon avalanche photo diode (Excelitas).

1.3. Diamond probe characterization

We use the same diamond probe for all the experiments presented in this work. We typically start our experiments by aligning the external bias field to the NV's symmetry axis. We proceed by determining the resonance frequency for one of the two spin transition $m_S = 0 \leftrightarrow m_S = \pm 1$ through optically detected magnetic resonance (ODMR) spectroscopy. Next, we determine the durations for $\pi/2$ and π pulses by measuring the Rabi oscillations as a function of microwave pulse length. To mitigate the effect of the ~ 3.1 MHz hyperfine splitting, we apply pulses exactly centered between the hyperfine peaks and aim for large Rabi frequencies, typically around $5 - 12$ MHz. Next, we record a spin echo or dynamical decoupling decay curve as detailed in Fig. S10(a) to select τ values at maxima of the spin echo revivals [41].

Finally, we determine the stand-off distance z between the NV center and the source of the magnetic signal (electrical current in our case) by scanning over the step edge of a thin film magnetic calibration sample (Pt/Co/AlOx). The expected magnetic field profile for this out-of-plane magnetized thin films is well understood [29] and can be fitted to the measured data. For the scanning NV tip used throughout this study, we determine a mean standoff distance of $z = 71$ nm, with a typical variation of ± 5 nm between the 8 different line scans (see Fig. S11).

2. CONVENTIONAL TRANSPORT MEASUREMENTS

2.1. Longitudinal and Hall resistance measurements

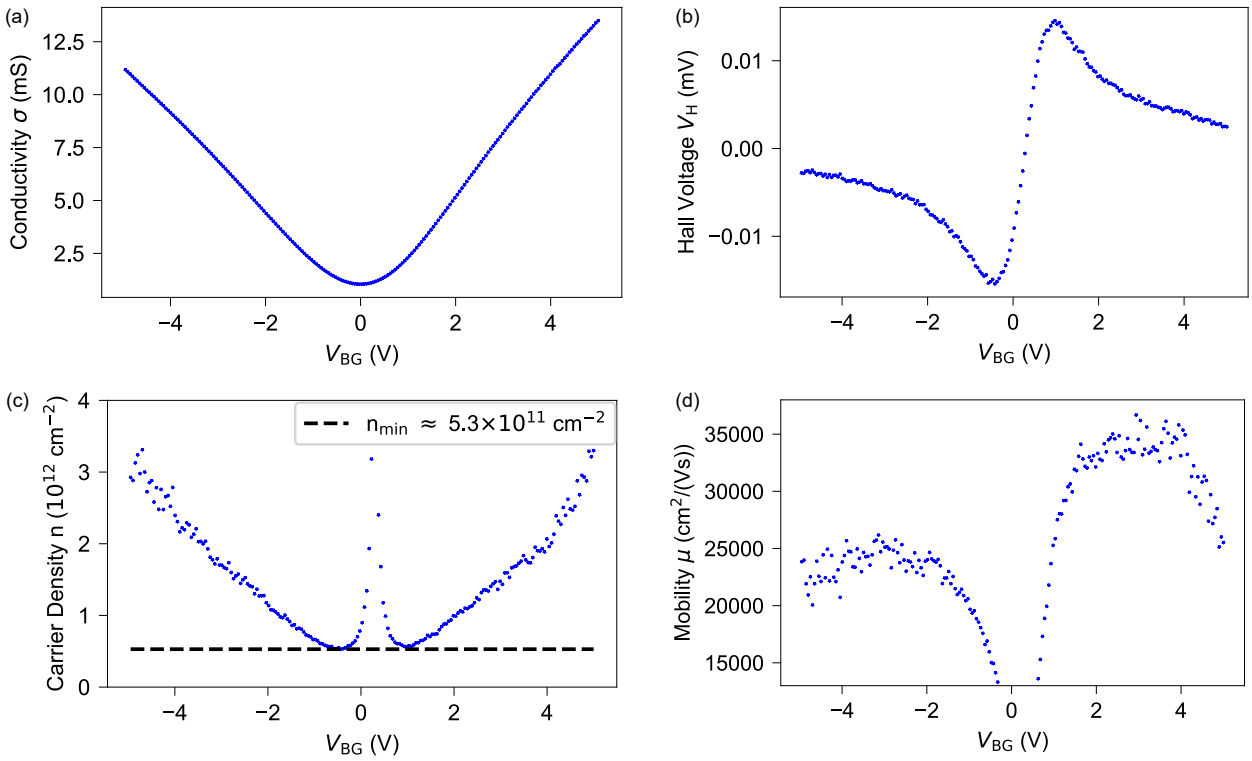

Figure S1. **Transport measurements.** Conductivity (a) and Hall voltage (b) as a function of the back-gate voltage V_{bg}. An out-of-plane field of $B = 37$ mT is applied. (c) Carrier density of the bilayer graphene sheet determined from the Hall measurement. An upper estimate for the residual carrier density at the charge neutrality point is indicated with the black dashed line. The model for the computation of the carrier density is not applicable close to the CNP. (d) Hall mobility versus back-gate voltage.

We use conventional transport measurements on the Hall-bar device (device B) to determine the conductivity σ, mobility μ and carrier density n as a function of the back-gate voltage. We send a constant current of approximately $I = 0.3$ μA through the main channel of the Hall-bar. A series resistor of 10 MΩ limits the current variations to approximately 1% as we sweep the back-gate voltage. We further monitor the current through the Hall-bar via a transimpedance amplifier (FEMTO DHPCA-100). All transport measurements are taken using lock-in amplifiers (Zurich Instruments HF2LI and MFLI) at a frequency of 127 Hz.

The longitudinal and transverse voltages are first amplified (×1000) before being measured by the lock-in amplifiers. For the data shown in Fig. S1, we applied an out-of-plane field of $B = 37$ mT.

We can directly compute the conductivity from the longitudinal voltage, the current I and the dimensions of the Hall-bar. In order to remove the geometric contribution to the transverse voltage (e.g. the signal obtained if one probe is closer to the source contact than the second), we take a second measurement at a lower magnetic field. Since the geometric contribution does not depend on the bias field, we can subtract this contribution to obtain the actual Hall voltage V_{H}, shown in Fig. S1(b). We can also determine the carrier density as well as the mobility for the sample under investigation (Fig. S1(c-d)):

$$n = \frac{B_z I}{e V_{\mathrm{H}}}$$
$$\mu = \frac{V_{\mathrm{H}} \sigma}{B_z I}$$

We note that the carrier density measurement is not reliable for voltages close to the charge neutrality point. Our simple model does not take into account the presence of two types of carriers. Therefore, it can only describe the regions where one carrier type is dominant. An upper bound to the residual carrier density at the charge neutrality point is given by the minimum of the measured carrier density $n_{\mathrm{min}} \approx 5.3 \times 10^{11}$ cm^{-2}.

2.2. Photo-doping

Throughout our experiments, we have observed effects of laser illumination on the transport characteristics of our devices. For example, on another Hall-bar structure with a graphite back-gate (device not shown), we have seen signatures of photo-induced doping reminiscent of the effects described in Ref. [21]. As can be seen in Fig. S2(a,b), the conductance of the device decreases over time when the sample is illuminated by the green laser and if it is tuned away from the CNP. Once the laser is turned off, the conductance recovers, albeit at a lower rate (Fig. S2(a)). This effect is attributed to the creation of charge traps in the bottom boron nitride layer [21]. To avoid this type of photo-induced doping during the laser readout, we have adapted the measurement scheme in our experiments. We first ramp the back-gate voltage to 0 V before performing the optical readout. Likewise, we have observed impacts of laser illumination on the sample presented in this publication

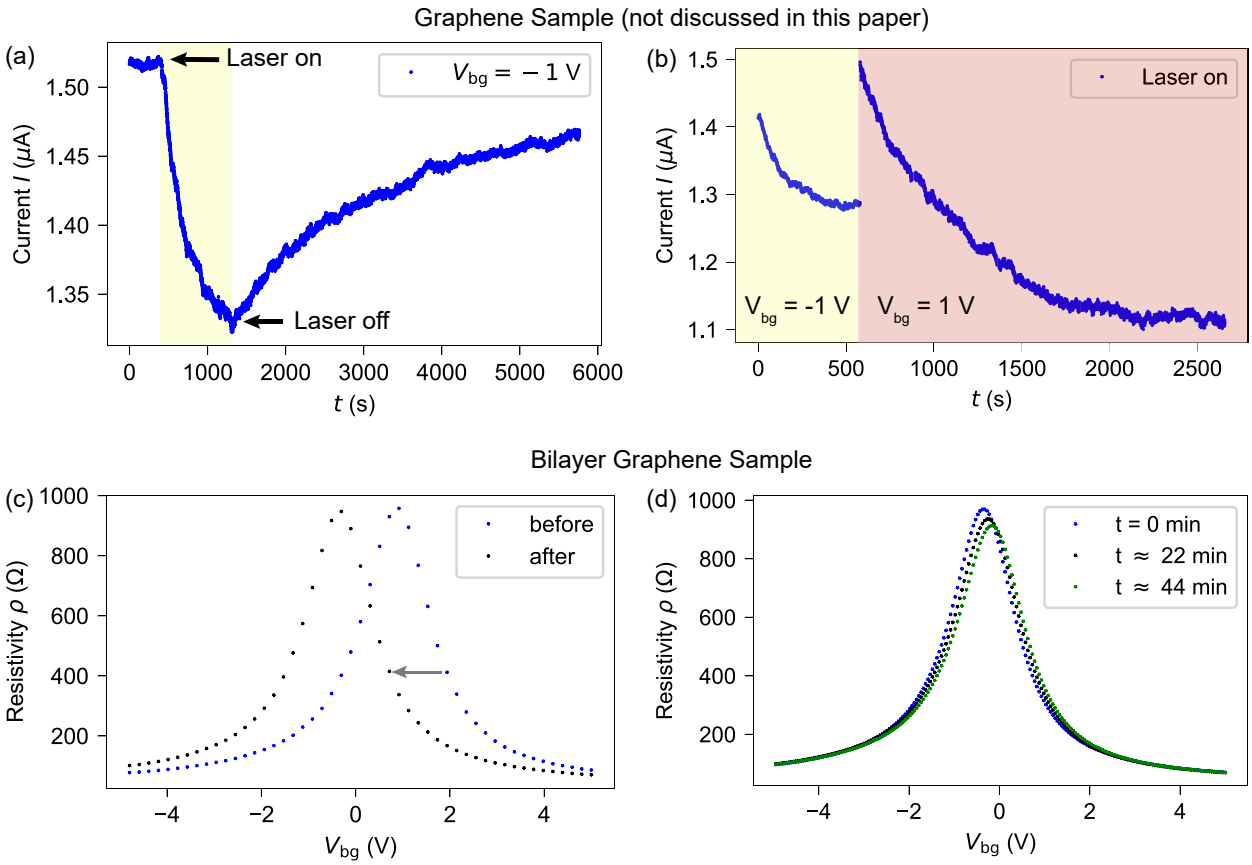

Figure S2. (a) Change of current flow through a graphene sample upon laser illumination. For the whole duration, the back-gate voltage is kept constant at $V_{bg} = -1$ V. (b) Similar experiment to (a) except that the sample is illuminated continuously and the back-gate voltage is changed. (c) Resistivity as a function of back-gate voltage before (blue dots) and after (black dots) laser illumination at $V_{bg} = 5$ V. d) Drift of the CNP over time in the absence of laser illumination (approximately $2 - 3$ minutes acquisition time per trace). Traces (a) and (b) were recorded on a graphene sample not discussed in this paper. (c) and (d) were measured on the device discussed within this publication.

(Fig. S2(c,d)). The observed shifts of the charge neutrality point are, however, not readily explained by the effect mentioned before. Again, setting the back-gate voltage to zero during the laser readout should make the experiments more reproducible and comparable.

3. QUANTUM PHASE MEASUREMENT

3.1. Phase accumulation under dynamical decoupling

For the following analysis, we assume that a sufficiently strong bias field $\mathbf{B}_0$ is applied parallel to the nitrogen-vacancy symmetry axis, such that we can neglect off-axis B fields from the device current and any electric interaction in the NV Hamiltonian [22]. The relevant part of the Hamiltonian in the lab frame is then given by $H = \hbar D \hat{S}_z^{\,2} + \hbar\gamma_e \left(B_0 + B(t)\right) \hat{S}_z$, with D denoting the zero-field splitting, B_0 a permanent magnetic field, $B(t)$ a time-varying magnetic field along the NV axis and $\hat{S}_z$ the Spin-1 z-operator. In the rotating frame at $\omega = D - \gamma_e B_0$, the Hamiltonian reads

$$\tilde{H} = \hbar\gamma_e B(t) \begin{pmatrix} 0 & 0 \\ 0 & -1 \end{pmatrix}$$

if we restrict our analysis to the $(|0\rangle, |-1\rangle)$ basis. If we initialize the NV spin into the superposition state $1/\sqrt{2}\left(|0\rangle + |-1\rangle\right)$ with a $\pi/2$ pulse and let it evolve for a duration τ, this state will evolve to $1/\sqrt{2}\left(|0\rangle + e^{i\phi}|-1\rangle\right)$, with the phase ϕ given by the integral:

$$\phi = \gamma_e \int_0^\tau B(t)\mathrm{d}t \tag{S1}$$

Consequently, for a constant magnetic field $B(t) = B_1$, a total phase $\phi = \gamma_e B_1 \tau$ is picked up by the sensor. We can now measure this phase by applying another $\pi/2$ pulse followed by an optical readout of the resulting population difference. In this case, the limitation to the magnetic field sensitivity is dependent on the dephasing time T_2^* of the sensor.

Fortunately, it is possible to delay the dephasing of the electronic spin state. This is achieved through the application of a series of equally-spaced π pulses during the phase evolution time. As result of this modification, Eq. (S1) no longer holds, and is now given by [33]:

$$\phi = \gamma_e \int_0^\tau \Theta(t) B(t)\mathrm{d}t.$$

The function $\Theta(t) = \pm 1$ modulates the relation between the accumulated phase and the B field by flipping sign upon each application of a π pulse. If we additionally modulate the polarity of a signal B_1 synchronously with the π-pulses, the product $B(t)\Theta(t) = B_1$ becomes constant. Here, B_1 is the amplitude of the square signal $B(t)$. Thus, the expression for the

accumulated phase simplifies to:

$$\phi = \gamma_e \int_0^\tau \Theta(t) B(t) \mathrm{d}t = \gamma_e B_1 \tau. \tag{S2}$$

With this measurement scheme, the maximum phase accumulation time is no longer limited by T_2^*, but rather by T_2, enabling measurements with improved magnetic field sensitivity. In the simplest experiment, a single π pulse is used (spin echo). Adding more pulses further decouples the spin from its magnetic environment and thus allows us to extend the sensing time and improve the magnetic field sensitivity of the protocol. A limiting factor is the imperfect nature of the applied π pulses. To improve the resilience of the spin state to these imperfections, a number of different measurement schemes have been developed [33]. For the experiments described within this publication, we have made use of the XY16 protocol to correct for pulse errors [56].

4. MAGNETIC FIELD SENSITIVITY

4.1. Analytical magnetic field sensitivity

In an AC sensing experiment, the photon signal C_Φ depends on the phase Φ of the final readout pulse via

$$C_\Phi = C_0 \left(1 - \frac{\epsilon}{2} + \frac{\epsilon e^{-(\tau/T_2)^\alpha}}{2} \cos(\gamma_e B_{\mathrm{ac}} \tau + \Phi)\right),$$

where C_0 is the photon count signal of the $m_S = 0$ spin state, ϵ is the NV contrast and τ the phase interaction time. The dephasing of the spin state is described by an exponential decay $\chi(\tau) = e^{-(\tau/T_2)^\alpha}$, with α taking values between 1 and 3 [57]. C_0 can be related to the photoluminescence rate I_0 of the $m_S = 0$ spin state via

$$C_0 = \frac{I_0 t_{\mathrm{coll}}}{t_{\mathrm{s}}} \cdot T_{\mathrm{exp}}$$

with $t_{\mathrm{coll}} = 0.3$ μs being the photon collection time, t_{s} the repetition time of the experiment and T_{exp} is the total dwell time per pixel. To resolve a magnetic field change δB_{ac}, we can pick the readout phase Φ that maximizes the photon signal change δC:

$$\delta C \approx \frac{I_0 t_{\mathrm{coll}}}{t_{\mathrm{s}}} \cdot T_{\mathrm{exp}} \cdot \frac{\epsilon e^{-(\tau/T_2)^\alpha}}{2} \gamma_e \tau \cdot \delta B_{\mathrm{ac}}$$

At a signal-to-noise ratio $\delta C / \sqrt{\langle C \rangle_\Phi} = \delta C / \sqrt{C_0 \left(1 - \frac{\epsilon}{2}\right)}$ of unity, we find for the magnetic field sensitivity:

$$\eta_B = \frac{1}{\gamma_e \tau} \frac{2}{\epsilon e^{-(\tau/T_2)^\alpha}} \sqrt{\frac{\left(1 - \frac{\epsilon}{2}\right) t_S}{I_0 t_{\mathrm{coll}}}}$$

For the probe parameters ($I_0 \approx 550\,\mathrm{kC/s}$, $\epsilon \approx 26\%$, $t_S = \tau + 4$ μs, $T_2 \approx 18$ μs, $\alpha \approx 0.9$ (Fit from Fig. S10)) we can numerically determine the optimal magnetic field sensitivity to be:

$$\eta_B \approx 66\ \mathrm{nT}/\sqrt{\mathrm{Hz}}$$

Correspondingly, for $N = 128$ refocusing pulses, $T_2 \approx 54$ μs and $\alpha \approx 1.2$ (Fit from Fig. S10), we find an optimal sensitivity of:

$$\eta_B \approx 32\ \mathrm{nT}/\sqrt{\mathrm{Hz}}$$

In a typical measurement including four readout phases, the sensitivity is worsened by a factor $\sqrt{2}$. Furthermore, for an experiment involving a phase acquisition time of $\tau = 38$ μs (as in Fig. 5(c-d) of the main text), we find a theoretical sensitivity of $\eta_B \approx 47\ \mathrm{nT}/\sqrt{\mathrm{Hz}}$.

4.2. Experimental magnetic field uncertainties

1. *Uncertainty from shot noise*

For a four-phase readout including the photon signals C_x, C_{-x}, C_y, C_{-y}, the accumulated phase can be computed with the two-argument arctangent function [12, 34]:

$$\phi_{\text{wrapped}} = \tan^{-1}\left(\frac{\pm(C_y - C_{-y})}{\pm(C_x - C_{-x})}\right).$$

The additional minus signs depend on the protocol used for sensing (e.g. Ramsey, Spin-echo, XYn). We can thus estimate the uncertainty in the phase signal to be

$$\sigma_\phi = \sqrt{\sum_{i=x,-x,y,-y}\left(\frac{\partial\phi_{\text{wrapped}}}{\partial C_i}\right)^2 \sigma_{C_i}^2}.$$

Assuming shot noise with $\sigma_{C_i}^2 = C_i$, we find:

$$\sigma_\phi = \sqrt{\left(\frac{C_y - C_{-y}}{(C_x - C_{-x})^2 + (C_y - C_{-y})^2}\right)^2 (C_x + C_{-x}) + \left(\frac{C_x - C_{-x}}{(C_x - C_{-x})^2 + (C_y - C_{-y})^2}\right)^2 (C_y + C_{-y})}$$

Taking into account that $C_y + C_{-y} = C_x + C_{-x} = (C_x + C_{-x} + C_y + C_{-y})/2$, it follows that

$$\sigma_\phi = \frac{1}{\sqrt{2}}\sqrt{\frac{C_x + C_{-x} + C_y + C_{-y}}{(C_x - C_{-x})^2 + (C_y - C_{-y})^2}}.$$

Given the relation between phase and magnetic field, we can thus determine the magnetic field uncertainty directly from the measured photon signals.

$$\sigma_B = \frac{1}{\sqrt{2}\gamma_e\tau}\sqrt{\frac{C_x + C_{-x} + C_y + C_{-y}}{(C_x - C_{-x})^2 + (C_y - C_{-y})^2}} \tag{S3}$$

We observed throughout multiple scans on two different devices that the NV signal contrast $\epsilon\chi(\tau)$ is changing as a function of tip position when using the Hahn echo protocol (Fig. S12). This leads to substantially increased phase uncertainties σ_ϕ, which in turn result in locally increased noise in the unwrapped magnetic field images. We have further observed that scanning with different acquisition times τ, but otherwise equal settings, does result in dissimilar signal contrast images. Consequently, an overall reduction of the spin coherence time can not be the sole explanation for this effect.

2. *Uncertainty from magnetic field map*

Alternatively, we can determine the magnetic field uncertainty of an image through an analysis of the noise in line-by-line differences. Ideally, this operation removes the magnetic field signal while retaining the magnetic field uncertainty. The magnetic field noise is however larger by a factor $\sqrt{2}$ due to the subtraction of two signals with the same assumed Gaussian noise distribution.

A comparison between this method and the former approach is shown in Fig. S3. The methods are tested on a data set consisting of several line scans, separated by 2 nm each. The data as well as the line-by-line differences are shown in Fig. S3(a-b). Fig. S3(c-d) furthers shows that the two methods yield comparable magnetic field uncertainties. The computation from the shot noise yields an uncertainty of $\sigma_B = 4.7 \pm 0.2$ nT whereas analyzing the line-by-line differences results in an uncertainty of $\sigma_B = 4.6$ nT

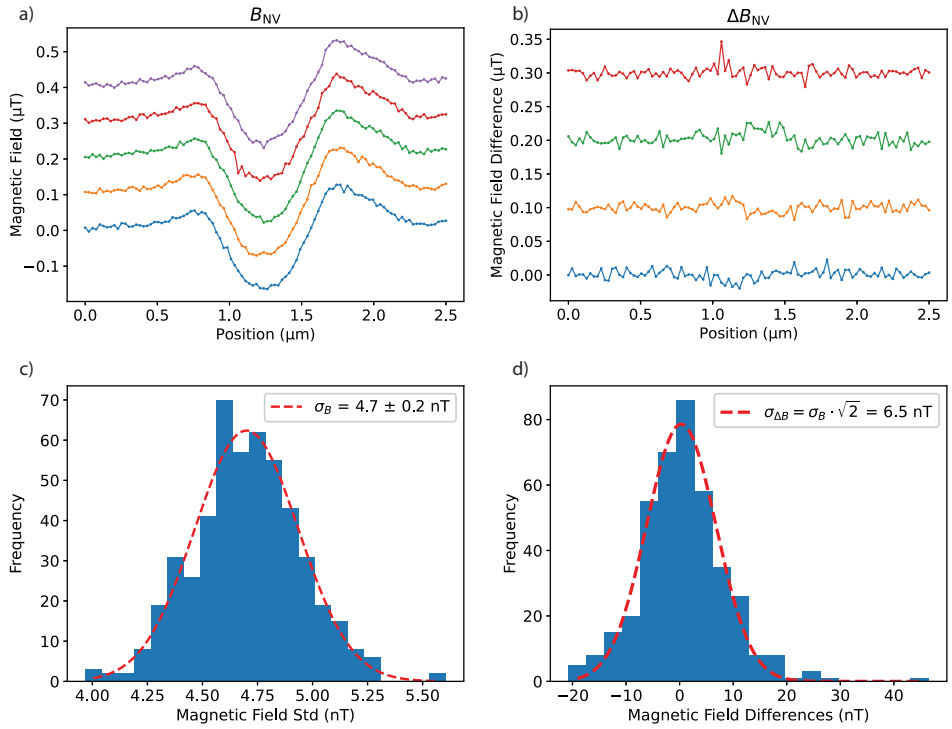

Figure S3. **Analysis of the magnetic field uncertainty** (a) Plot of the magnetic field scans and (b) the corresponding numerically computed line-by-line differences. The individual traces have been shifted by 0.1 μT. (c) Histogram of the uncertainties extracted from the photon signals [Eq. (S3)]. (d) Histogram of the magnetic field differences shown in (b). The dashed red lines are Gaussian fits to the histograms.

5. PHASE UNWRAPPING ALGORITHMS

5.1. Variable grid size method

Here, we describe the procedure to reconstruct the magnetic field image from multiple images with varying pixel resolution. The phase images shown in the left column of Fig. S4 were acquired within 72 hours of measurement time with the majority of time spent on the middle scan (41 hours). For the three images, each pixel has been imaged for a total of five seconds using the Hahn echo protocol ($\tau = 18$ μs). Image resolutions are 60×60 pixels in a 6 μm $\times$ 6 μm area (top row), 160×120 pixels in a 3 μm $\times$ 4 μm area (middle row), and 100×100 pixels in 2 μm $\times$ 1 μm area (bottom row). We process our data using a similar approach as described in Ref. [11], adapted for phase data:

1. We start by unwrapping the three phase images using the *unwrap_phase* function provided by the *scikit-image* python library [37] (see Fig. S4(a)).

2. We proceed by re-sampling the three magnetic field maps onto a common 20 nm$\times$20 nm pixel grid through linear interpolation.

3. All three images are now combined into a single magnetic field image. We start with the low-resolution image (top) and replace areas that have been scanned at a higher spatial resolution. We did not need to correct for drifts in the xy-plane between images, as they are barely visible in the resulting image.

5.2. Bayesian inference method

In the following section, we describe the algorithm used to estimate the magnetic field map above a current-carrying sample by combining the information stored in two phase-wrapped images. The magnetic field signal seen by the NV center is the same for both images, but is encoded differently due to the varying phase acquisition times (see Eq. (S2)). To extract this information, we perform the following steps:

1. We start by extending the original images by 10 pixels in each direction, with reflecting boundary conditions (not shown in Fig. S5). This step reduces potential boundary effects in the subsequent steps. We then compute the residues of the two images

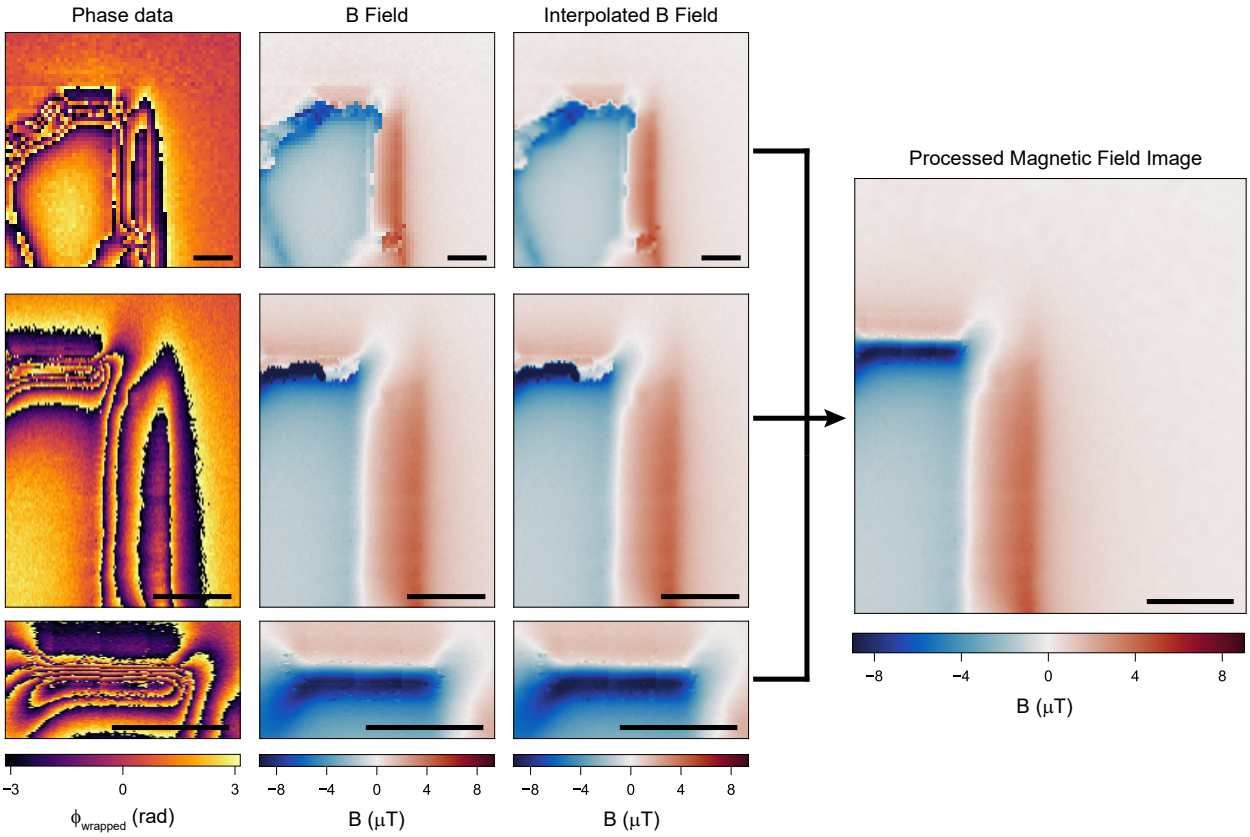

Figure S4. **Multi-image processing flow diagram.** Three phase images with different spatial resolution (first column) were acquired and subsequently unwrapped (second column). A new magnetic field map is generated via interpolation of the existing magnetic field data onto a new common finer grid (third column). All three processed images are then combined into a single image (fourth column). All scale bars are 1 μm.

(smallest closed line integrals of the wrapped phase differences, e.g. along the edges of 2x2 pixel boxes) [35]. Finding a non-vanishing residue means that phase unwrapping might become difficult in the vicinity. Therefore, we keep track of all the pixels involved in the computation of the non-vanishing residues (see Fig. S5(b)). Finally, we identify an area (delimited by the red line in Fig. S5(b)) enclosing all the problematic pixels of the two phase images. The Bayesian inference method will only operate on the pixels within this region.

2. The two images are then partially unwrapped using the *unwrap_phase* method from the *scikit-image* package [37], leaving the problematic areas wrapped for the moment. The corresponding magnetic field images are displayed in Fig. S5(c).

3. A first estimate of the magnetic field seen by the NV center is generated as follows. For the area where phase unwrapping works well in both images (reliable pixels), we compute the inverse-variance weighted average of the two images. For each of the remaining pixels (unreliable pixels), we generate a magnetic field probability distribution $P(B) = P_1(B) \cdot P_2(B)$ (S5(d) bottom plot) by multiplying the respective probability distributions (S5(d) left and right plot)

$$P_i(B) = \frac{1}{C_i} \sum_{k=-k_{\mathrm{max,i}}}^{k_{\mathrm{max,i}}} \exp\left(-\frac{\left[(\phi_i + 2\pi k)/(\gamma_e \tau_i)\right]^2}{2\sigma_i^2} \right) \; ; \; i = 1, 2$$

and taking the most likely magnetic field value of the result as initial estimate [42, 43]. C_i is a normalization constant, ϕ_i is the measured wrapped phase, γ_e is the gyromagnetic ratio, τ_i is the phase accumulation time, σ_i is the magnetic field uncertainty extracted from the measured photon signals, and k is number of phase wraps. The resulting image is shown in Fig. S5(e). For the data presented in Figs. S5 and S6 (three data sets with varying currents), we restrict ourselves to the magnetic field range $[-15\ \mu\mathrm{T} : 15\ \mu\mathrm{T}]$, which sets $k_{\mathrm{max},1} = 4$ and $k_{\mathrm{max},2} = 9$.

4. We now iterate through all the unreliable pixels, starting with the ones closest to the reliable pixels. We compute estimates for the magnetic field at each pixel via:

   - a mean of the neighboring pixels
   - 4× linear extrapolation along the grid directions, e.g. in positive x-direction:

   $$B_{i,j} = B_{i-1,j} + (B_{i-1,j} - B_{i-2,j})$$

   - 4× linear extrapolation based on the corner pixels, e.g. for the bottom left corner:

   $$B_{i,j} = B_{i-1,j} + B_{i,j-1} - B_{i-1,j-1}$$

   For each of the nine estimates, we determine the uncertainty by propagating the uncertainties of the involved pixel values. These are either directly given for the reliable pixels (extracted from the photon signals) or can be computed by evaluating the variance of the probability distribution for the unreliable pixels. In a last step, we compute the final estimate B_{est} by taking the inverse-variance weighted average of the aforementioned estimates. We then generate a normal probability distribution

centered around this estimate with a width σ proportional to the error of the final estimate:

$$\sigma = \sigma_0 \cdot \sqrt{\frac{\mathrm{Var}(B_{\mathrm{est}})}{\mathrm{Var}(B_{\mathrm{img}})}}$$

The parameter σ_0 can be freely chosen and determines how quickly unlikely solutions are rejected during the iterative update process. For the data shown in this paper, we chose $\sigma_0 = 350$ nT. The variance $\mathrm{Var}(B_{\mathrm{img}})$ is the mean variance of all the reliable pixels. Finally, we update a pixel's probability distribution by multiplying it with this Gaussian distribution. This step narrows down the set of possible solutions, as illustrated in Fig. S5(f).

5. Step 4 is repeated until the variance of the probability function for each pixel is not changing significantly any more($\leq 0.1\%$ relative change). The iterative process is visualized in Fig. S5(g).

In the regions where the magnetic field image is computed through inverse-variance weighting, the resulting theoretical magnetic field uncertainty is given by

$$\sigma_B = \frac{\sigma_1}{\sqrt{1+\sigma_1^2/\sigma_2^2}} = \frac{\sigma_2}{\sqrt{1+\sigma_2^2/\sigma_1^2}} \ . \tag{S4}$$

For the data set shown in the main text, we have determined the magnetic field uncertainties to be $\sigma_1 = 66$ nT and $\sigma_2 = 40$ nT using equation S3. We would therefore expect:

$$\sigma_B = 34 \text{ nT}$$

This is in good agreement with the magnetic field uncertainty of $\sigma_B = 37$ nT extracted from line-by-line differences in a region without signal. Note that this uncertainty lies in between the uncertainty that would have resulted from imaging the entire time at $\tau = 10$ μs (≈ 40 nT) and $\tau = 20.5$ μs (≈ 31 nT), demonstrating that acquiring multiple images with different τ does not increase the nominal sensitivity. It does however ameliorate phase unwrapping difficulties without sacrificing too much magnetic field sensitivity. Recording more than two images with differing phase acquisition times τ would make the phase unwrapping algorithm more robust. Note that the above algorithm can in principle also be used on a single phase image.

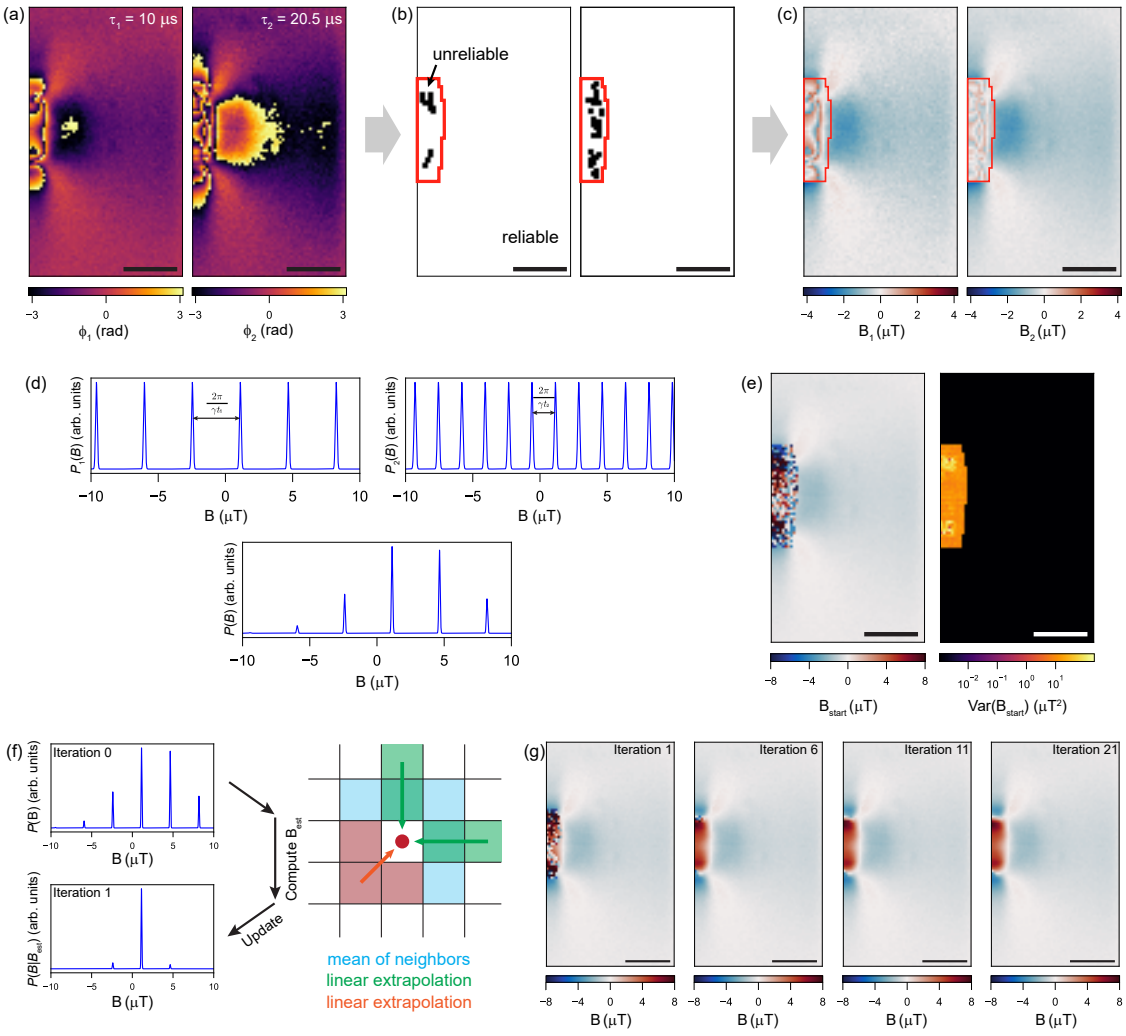

Figure S5. **Processing of two simultaneously recorded phase images.** (a) Phase images with acquisition times of $\tau = 10$ μs and $\tau = 20.5$ μs. (b) Map of the residues (black pixels) and area of unreliable pixels (delimited by the red line). (c) Partially unwrapped magnetic field maps. (d) Magnetic field probability distributions for a pixel in the area delimited by the red line in (b) (left and right plot) and joint probability distribution for the same pixel (bottom plot). (e) Magnetic field and variance map obtained by combining the two data sets. (f) Visualization of the update rule for the magnetic field probability distribution in a single iteration of the phase estimation algorithm for a single pixel. Some of the pixels involved in the computation of the estimate B_{est} are indicated in the schematic on the right: neighbor mean (blue), 2 (out of 4) extrapolations along the grid axes (green) and 1 (out of 4) extrapolations using the corner values (orange). (g) Field estimate progression for different steps during the iterative process. Scale bars are 1 μm.

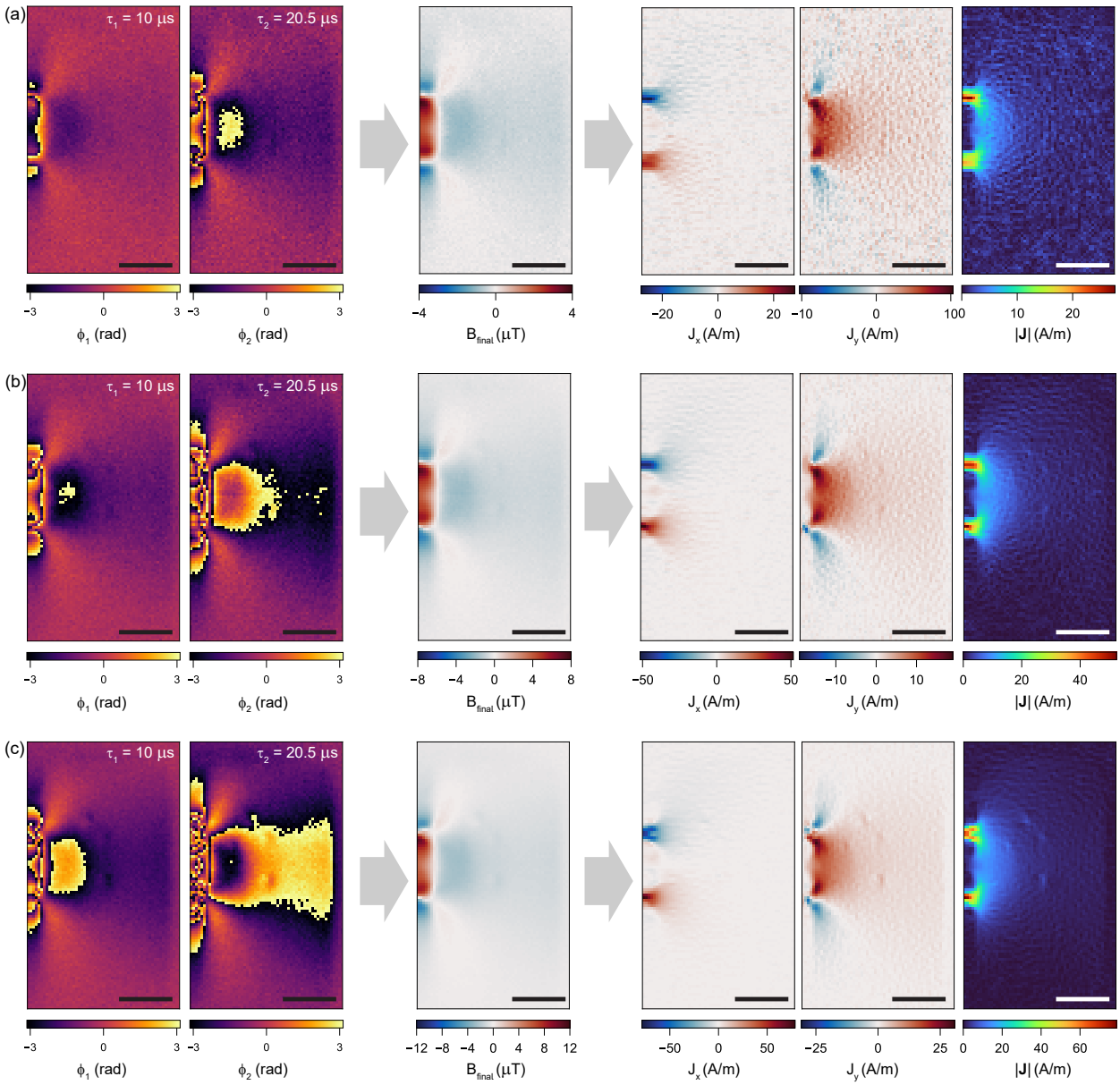

Figure S6. **Output of the phase estimation algorithm for three data sets.** For all three data sets, the two phase images are shown on the left, the reconstructed phase image is shown in the middle, and the current density images are shown on the right ($\lambda = z$). (a) Data set with $I \approx 5.3$ μA. (b) Data set presented in the main text of this publication. $I \approx 10$ μA (c) Data set with $I \approx 13.4$ μA. All scale bars are 1 μm.

6. CURRENT DENSITY RECONSTRUCTION

We convert magnetic field images into current distributions by inverting the Biot-Savart law in Fourier space. A more extensive discussion of the inverse filtering technique and the exact relation between the Fourier transforms $\mathcal{F}[\mathbf{J}]$ and $\mathcal{F}[B_{\mathrm{NV}}]$ is discussed in Refs. [15, 39, 40]:

$$J_x(k_x,k_y,z) = -\frac{2}{\mu_0}\frac{k_y e^{kz}}{n_x k_x + n_y k_y + i n_z k} w(k,\lambda) B_{\mathrm{NV}}(k_x,k_y)$$
$$J_y(k_x,k_y,z) = \frac{2}{\mu_0}\frac{k_x e^{kz}}{n_x k_x + n_y k_y + i n_z k} w(k,\lambda) B_{\mathrm{NV}}(k_x,k_y)$$

Here, k_x, k_y denote spatial frequency coordinates and $k = \sqrt{k_x^2 + k_y^2}$. The Hann window function $w(k,\lambda) = \cos^2(k\lambda/4) \cdot H(2\pi/\lambda - k)$ is responsible for attenuating noisy high spatial frequency components, at the expense of reducing the spatial resolution of the resulting current density image. In the latter equation, $H(k)$ is the Heaviside function, and λ is the spatial filtering parameter. The orientation of the NV center is given by the vector $\mathbf{n} = (\cos\varphi\sin\theta, \sin\varphi\sin\theta, \cos\theta)$. We use the following convention for the Fourier transform: $J_x(k_x,k_y,z) = \int_{-\infty}^{\infty}\int_{-\infty}^{\infty} J_x(x,y,z) e^{-ik_x x - ik_y y} \mathrm{d}x\mathrm{d}y$. The datasets are expanded during the reconstruction process to avoid artifacts due to magnetic field truncation [15, 40]. For the data sets presented in this publication with perpendicular current injectors, we found that extending the edge values (e.g. to a 3× or 9× larger image) worked well on our data.

7. SPATIAL ANALYSIS OF CURRENT DENSITY MAPS

7.1. Local variations in the current density

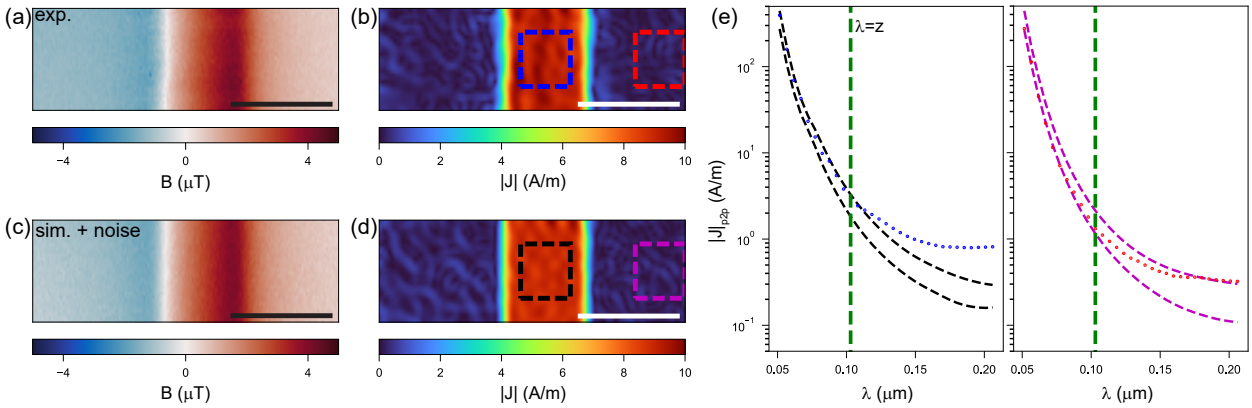

Figure S7. **Analysis of current density profiles.** (a) Magnetic field map recorded above the Hall-bar structure (device B). (b) Reconstructed current density magnitude for $\lambda = 1.25 \cdot z$. (c) Simulated magnetic field map with added Gaussian noise and (d) reconstructed current density. (e) Plot of the peak-to-peak variations of $|\mathbf{J}|$ versus spatial filtering parameter in the areas delimited by the boxes in (b) and (d). The left plot displays variations of the current density on top of the conductor, and the right plot shows variations next to it. The dashed lines correspond to $\langle |\mathbf{J}|_{\mathrm{p2p}} \rangle \pm 2\sigma$. Scale bars are 1 μm.

We want to investigate whether there are small modulations on top of the rectangular current profile shown in Fig. 3(c) of the main text. Therefore, we will analyze a subsection of the presented data set. The B field along with an example of the reconstructed current density is shown in Fig. S7(a-b). What we are interested in are the variations in the area enclosed by the blue dashed lines. Precisely, we want to know whether the variations of the current density are caused by an actual signal, e.g. a local variation of current flow, or whether they are caused by the reconstruction algorithm. The latter is the case in the area delimited by the red dashed rectangle. Inverting the law of Biot-Savart introduces noise at high spatial frequencies and therefore filtering is necessary [39]. We can therefore vary λ to suppress the reconstruction artifacts. To create comparable data, we generate 2000 simulated data sets by assuming a uniform current density profile in an 800 nm wide stripe, then evaluate the corresponding magnetic field image and add Gaussian noise on top of

the B field data. These simulated B field images are then reconstructed individually and the peak-to-peak variations of $|\mathbf{J}|$ are measured both on top and outside of the stripe. To generate a comparable data set, offsets in J_x and J_y (that cannot be reconstructed via the inverse filtering technique [39]) have been subtracted. A region where no current can flow has been analyzed for this purpose. Examples are shown in Fig. S7(c-d). Evaluating many simulated data sets allows us to create an upper and lower bound for the expected peak-to-peak variations. Fig. S7(e) summarizes the analysis; the fluctuations of the current density within the stripe sit outside the $\pm 2\sigma$ range generated by the simulations. The fluctuation outside the stripe however, fall mostly within the range generated by noise. This is an indication that there are local variations within the approximately uniform current density – the feature shown in Fig. 4(c) of the main text is most likely not caused by random noise.

7.2. Differential imaging

Fig. S8(a) displays the magnetic field data acquired in the differential imaging scan for $V_{\mathrm{bg}} = -2$ V and $V_{\mathrm{bg}} = 0$ V. For these measurements, $\tau = 24$ μs, n = 16 pulses and $V_{\mathrm{sd}} = 65$ mV. A numerical B field difference can be computed (Fig. S8(b)) and subsequently reconstructed ($\lambda = 175.5$ nm). The resulting current densities J_x and J_y are shown in Fig. S8(c). Due to the linearity of the inverse filtering technique, reconstructing the current densities first, followed by numerical subtraction of the current densities gives exactly the same result. The current density image ΔJ_y shows convincingly that the back-gated region is more conductive at $V_{\mathrm{bg}} = -2$ V. The interpretation of the ΔJ_x image is more intricate as there seems to be a spatially constant term masking the real signal.

7.3. Line scans across the Hall-bar

The inverse filtering technique assumes that the magnetic field map is measured in a constant plane above the sample. This is indeed the case for almost all the data shown in this publication, with the exception of a few line scans recorded above the Hall-bar (see Fig. 4(f) of the main text). For these line scans, the NV-graphene distance varies as the scanning tip follows the topography of the sample. We will separately analyze these line scans and show that the measured data is well explained by a rectangular current profile. The magnetic field

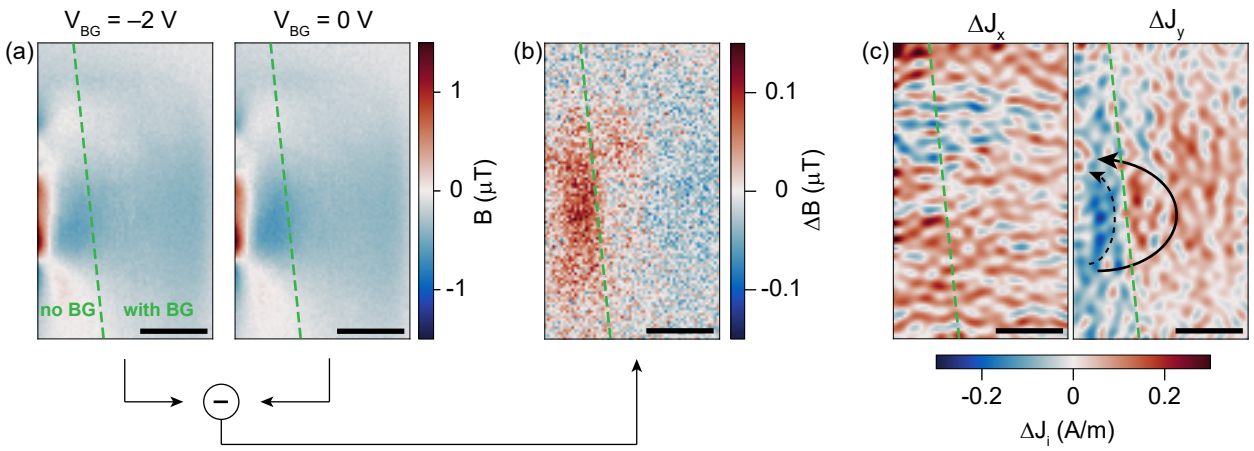

Figure S8. **Differential back-gate scans.** (a) Two magnetic field maps with back-gate voltage $V_{\mathrm{BG}} = -2\,\mathrm{V}$ and $V_{\mathrm{BG}} = 0\,\mathrm{V}$, respectively. The green dashed line indicates the edge of the graphite back-gate. (b) Differential magnetic field map $\Delta B = B_{(V_{\mathrm{BG}}=-2\,\mathrm{V})} - B_{(V_{\mathrm{BG}}=0\,\mathrm{V})}$ obtained by pixel-by-pixel subtraction of the two images. (e) Current density components ΔJ_x and ΔJ_y reconstructed from (d) ($\lambda = 175.5$ nm). Slightly higher current density is observed in the back-gated region (bold arrow), consistent with a higher carrier density and conductivity at finite doping.

generated by a stripe carrying a uniform current can be computed analytically; for a uniform current density J_y between positions x_1 and x_2, we find for the magnetic field components at a distance h :

$$B_x = -\frac{2\mu_0 J_y}{4\pi}\left(\arctan\frac{x-x_2}{h} - \arctan\frac{x-x_1}{h}\right)$$

$$B_y = 0$$

$$B_z = \frac{\mu_0 J_y}{4\pi}\ln\frac{(x-x_2)^2+h^2}{(x-x_1)^2+h^2}$$

The projection onto the symmetry axis of the NV center is given by $B_{\mathrm{NV}} = \mathbf{B}\cdot\mathbf{n}(\theta,\varphi)$, with $\mathbf{n}(\theta,\varphi)$ describing the orientation of the NV center. Fig. S9(a) displays the expected magnetic field map as a function of the NV-graphene distance (Fig. S9(b)). We can then create a model for the measured B-field image by picking the magnetic field value corresponding to the NV-graphene distance at each point along the line scan. This will result in a one dimensional profile that depends on the position of the stripe (x_1, x_2), the current density component J_y, and the two NV angles θ and φ. A fit of this model to the measured data is shown in Fig. S9(c). We can further reconstruct both the data and the model using the inverse filtering technique (Fig. S9(d)). Since the two curves include height changes at this

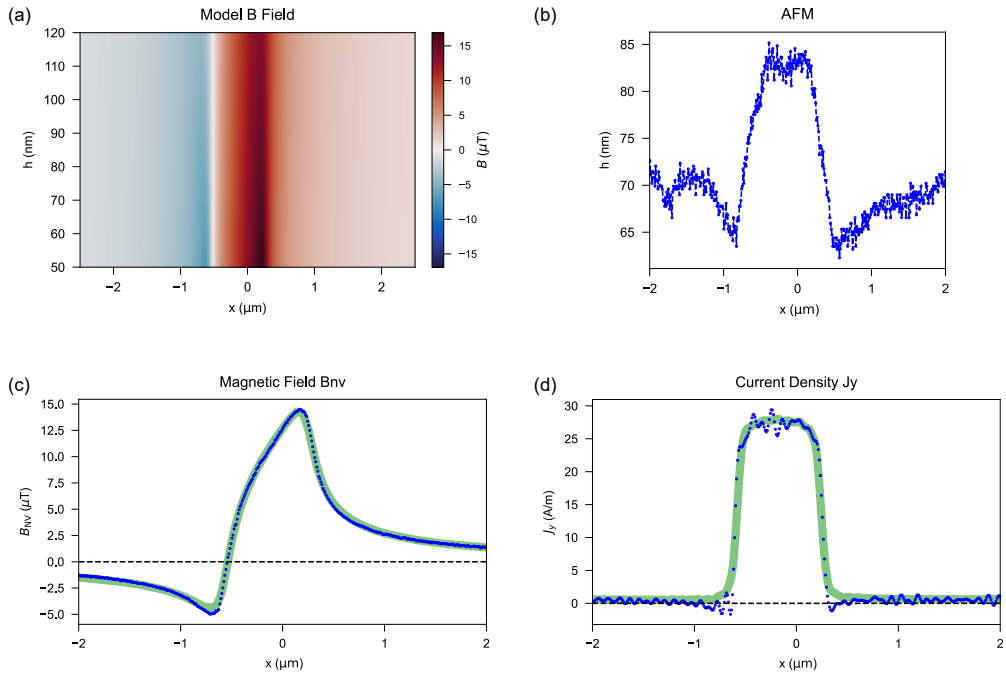

Figure S9. **Fitting current profiles.** (a) Map of the magnetic field projection B_{NV} above a stripe carrying a uniform current as a function of x and h ($x_1 = -0.59$ μm, $x_2 = 0.24$ μm, $J_y = 29\,\mathrm{A/m}$, $\theta = 50.5\,^\circ$ and $\varphi = 139.0\,^\circ$). (b) Distance between the NV center and the current-carrying layer while scanning across the Hall-bar (device B). (c) The measured B field (blue dots) along with the fit to the data (thick green line) for a line scan across the Hall-bar. (d) The reconstructed ($\lambda = 71\,\mathrm{nm}$) current density component J_y for the measured data (blue dots) and the fitted model (thick green line).

point, the reconstructed current densities can be compared. By analyzing both the magnetic field data and the current density images, we come to the conclusion, that our data is well explained by a uniform current profile through the Hall-bar. For the data traces shown in Fig. 4(f) of the main text with $I_{\mathrm{SD}} < 23.5$ μA, the model for the current density (Fig. S9(d)) has been rescaled according to the current flow through the device.

8. ADDITIONAL FIGURES

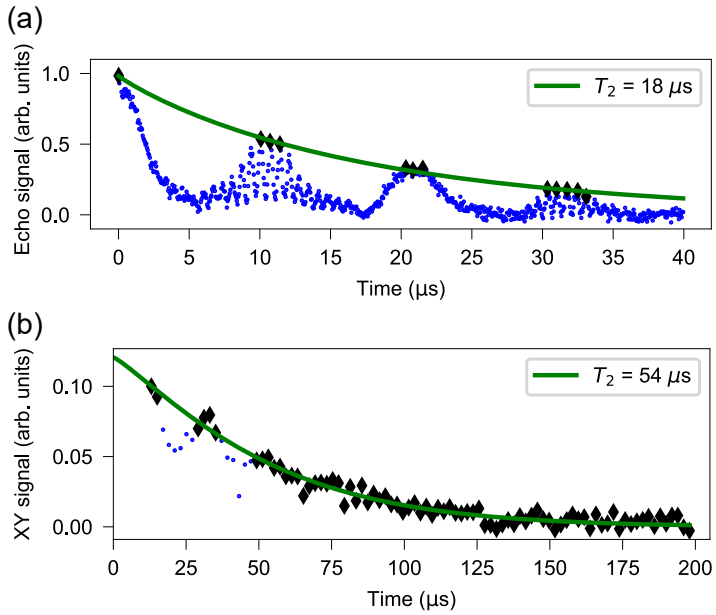

Figure S10. T_2 **measurements** (a) Spin-echo experiment (N=1) at a bias field of 17.7 mT. We fit the envelope (black diamonds) with an exponential decay function (green line) to extract T_2. (b) Dynamical decoupling experiment with N=128 pulses (8 × XY16). The envelope is again fitted with an exponential decay function. Further details regarding the fits are discussed in section 4.

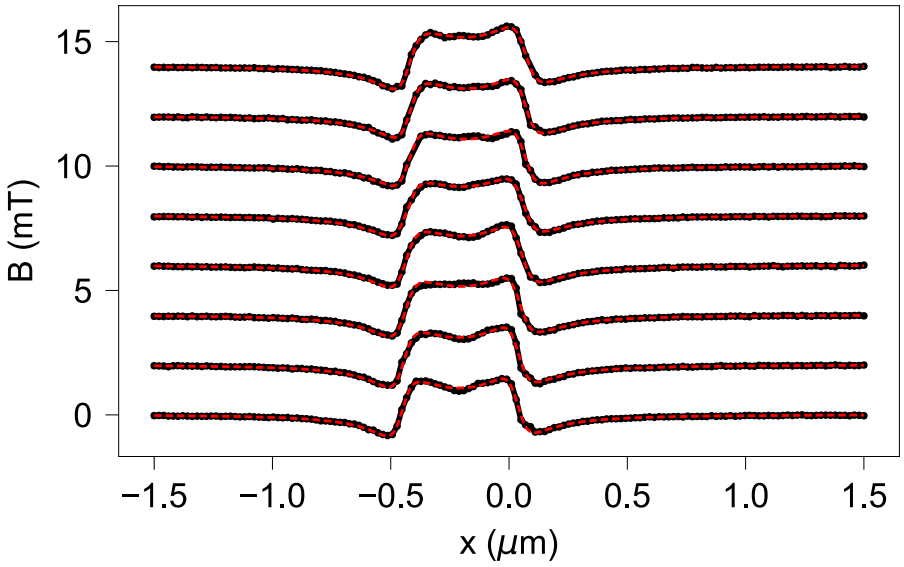

Figure S11. **Line scans across the magnetic calibration sample.** The individual lines are offset by 2 mT for clarity. The data (blue dots) is fitted with a model describing the perpendicularly magnetized sample (red dashed line).

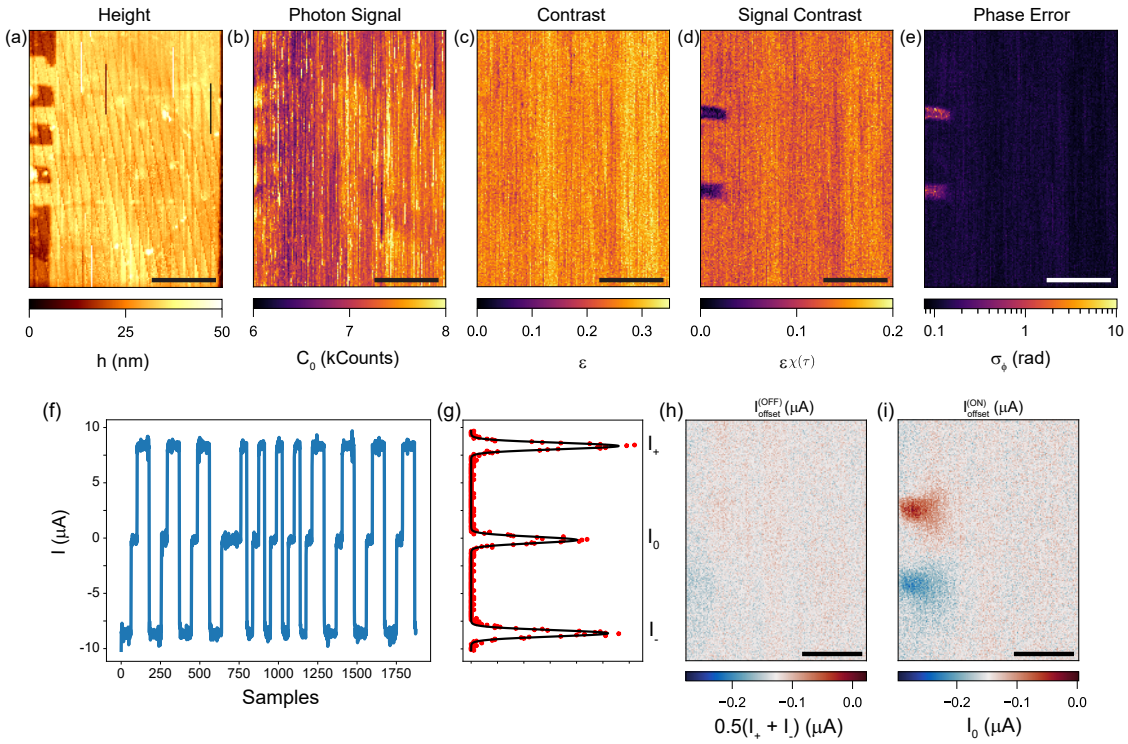

Figure S12. **Additional measurement channels recorded during a magnetometry scan.** (a) AFM topography image recorded with the diamond scanning probe. (b) Photon signal C_0 of the $m_S = 0$ state, measured additionally to the four phase readouts. (c) NV contrast as well as the (d) signal contrast as a function of tip-position. The signal contrast $\epsilon\chi(\tau)$ is severely reduced near the current injectors. (e) Phase uncertainty computed from the four recorded photon signals using equation (S3). Since the photo-luminescence as well as the contrast of the NV center are only weakly position-dependent, they cannot cause the increased phase noise near the injectors. As shown in the main text, the Rabi frequency is not changing significantly as a function of tip position. Therefore, we believe that this apparent reduction of coherence is not caused by improper pulses. (f) Current trace recorded during the magnetometry scan. The sampling rate is 7.5 MSa/s. (g) Histogram of the current trace. The histogram is fitted with a sum of three Gaussians centered around I_+, I_-, and I_0. (h-i) Unprocessed maps for $I^{\mathrm{OFF}}_{\mathrm{offset}}$ (h) and $I^{\mathrm{ON}}_{\mathrm{offset}}$ (i) introduced in the main text. For the ON image, the laser is turned on approximately 60 % of the time, thus some averaging is taking place. For the maps shown in the main text, a constant offset of $I = -0.11$ μA (h), and $I = -0.13$ μA (i) have been subtracted. These constant offset do not seem to correlate with the device structure and are likely hardware-related. Scale bars are 1 μm.

[11] A. Jenkins, S. Baumann, H. Zhou, S. A. Meynell, D. Yang, K. Watanabe, T. Taniguchi, A. Lucas, A. F. Young, and A. C. B. Jayich, Imaging the breakdown of ohmic transport in graphene, arXiv:2002.05065 (2020).

[12] M. J. H. Ku, T. X. Zhou, Q. Li, Y. J. Shin, J. K. Shi, C. Burch, L. E. Anderson, A. T. Pierce, Y. Xie, A. Hamo, U. Vool, H. Zhang, F. Casola, T. Taniguchi, K. Watanabe, M. M. Fogler, P. Kim, A. Yacoby, and R. L. Walsworth, Imaging viscous flow of the Dirac fluid in graphene, Nature **583**, 537 (2020).

[15] K. Chang, A. Eichler, J. Rhensius, L. Lorenzelli, and C. L. Degen, Nanoscale imaging of current density with a single-spin magnetometer, Nano Letters **17**, 2367 (2017).

[21] L. Ju, J. Velasco, E. Huang, S. Kahn, C. Nosiglia, H.-Z. Tsai, W. Yang, T. Taniguchi, K. Watanabe, Y. Zhang, G. Zhang, M. Crommie, A. Zettl, and F. Wang, Photoinduced doping in heterostructures of graphene and boron nitride, Nature Nanotechnology **9**, 348 (2014).

[22] L. Rondin, J. P. Tetienne, T. Hingant, J. F. Roch, P. Maletinsky, and V. Jacques, Magnetometry with nitrogen-vacancy defects in diamond, Rep. Prog. Phys. **77**, 056503 (2014).

[25] L. Wang, I. Meric, P. Y. Huang, Q. Gao, Y. Gao, H. Tran, T. Taniguchi, K. Watanabe, L. M. Campos, D. A. Muller, J. Guo, P. Kim, J. Hone, K. L. Shepard, and C. R. Dean, One-dimensional electrical contact to a two-dimensional material, Science **342**, 614 (2013).

[26] P. J. Zomer, M. H. D. Guimarães, J. C. Brant, N. Tombros, and B. J. van Wees, Fast pick up technique for high quality heterostructures of bilayer graphene and hexagonal boron nitride, Applied Physics Letters **105**, 013101 (2014).

[29] T. Hingant, J.-P. Tetienne, L. Martínez, K. Garcia, D. Ravelosona, J.-F. Roch, and V. Jacques, Measuring the Magnetic Moment Density in Patterned Ultrathin Ferromagnets with Submicrometer Resolution, Physical Review Applied **4**, 014003 (2015).

[30] QZabre AG, https://qzabre.com.

[33] C. Degen, F. Reinhard, and P. Cappellaro, Quantum sensing, Rev. Mod. Phys. **89**, 035002 (2017).

[34] H. S. Knowles, D. M. Kara, and M. Atature, Demonstration of a coherent electronic spin cluster in diamond, Phys. Rev. Lett. **117**, 100802 (2016).

[35] D. C. Ghiglia and M. D. Pritt, *Two-dimensional phase unwrapping: theory, algorithms, and software* (Wiley, New York, 1998).

[37] S. van der Walt, J. L. Schönberger, J. Nunez-Iglesias, F. Boulogne, J. D. Warner, N. Yager, E. Gouillart, T. Yu, and the scikit-image contributors, scikit-image: image processing in Python, PeerJ **2**, e453 (2014).

[39] B. J. Roth, N. G. Sepulveda, and J. P. Wikswo, Using a magnetometer to image a two-dimensional current distribution, J. Appl. Phys. **65**, 361 (1989).

[40] D. Broadway, S. Lillie, S. Scholten, D. Rohner, N. Dontschuk, P. Maletinsky, J.-P. Tetienne, and L. Hollenberg, Improved current density and magnetization reconstruction through vector magnetic field measurements, Phys. Rev. Applied **14**, 10.1103/physrevapplied.14.024076 (2020).

[41] L. Childress, M. V. G. Dutt, J. M. Taylor, A. S. Zibrov, F. Jelezko, J. Wrachtrup, P. R. Hemmer, and M. D. Lukin, Coherent dynamics of coupled electron and nuclear spin qubits in diamond, Science **314**, 281 (2006).

[42] N. M. Nusran, M. U. Momeen, and M. V. G. Dutt, High-dynamic-range magnetometry with a single electronic spin in diamond, Nat. Nanotechnol. **7**, 109 (2012).

[43] G. Waldherr, J. Beck, P. Neumann, R. S. Said, M. Nitsche, M. L. Markham, D. J. Twitchen, J. Twamley, F. Jelezko, and J. Wrachtrup, High-dynamic-range magnetometry with a single nuclear spin in diamond, Nat. Nanotechnol. **7**, 105 (2012).

[56] T. Gullion, D. B. Baker, and M. S. Conradi, New, compensated Carr-Purcell sequences, J. Magn. Res. **89**, 479 (1990).

[57] Y. Romach, C. Muller, T. Unden, L. Rogers, T. Isoda, K. Itoh, M. Markham, A. Stacey, J. Meijer, S. Pezzagna, B. Naydenov, L. McGuinness, N. Bar-Gill, and F. Jelezko, Spectroscopy of surface-induced noise using shallow spins in diamond, Phys. Rev. Lett. **114**, 017601 (2015).